Deep-Sea Research II 93 (2013) 119–134

Contents lists available at SciVerse ScienceDirect

Deep-Sea Research II

journal homepage: www.elsevier.com/locate/dsr2

Physical and biological controls of nitrate concentrations in the upper subtropical North Pacific Ocean

François Ascani [a,b,*], Kelvin J. Richards [a,b], Eric Firing [a], Scott Grant [a], Kenneth S. Johnson [c], Yanli Jia [b], Roger Lukas [a], David M. Karl [a,d]

[a] School of Ocean and Earth Science and Technology, Department of Oceanography, University of Hawaii at Manoa, 1000 Pope Road, Honolulu, HI 96822, USA
[b] School of Ocean and Earth Science and Technology, International Pacific Research Center, University of Hawaii at Manoa, 1680 East West Road, Honolulu, HI 96822, USA
[c] Monterey Bay Aquarium Research Institute, Moss Landing, CA 95039, USA
[d] School of Ocean and Earth Science and Technology, Center for Microbial Oceanography: Research and Education, University of Hawaii at Manoa, 1950 East West Road, Honolulu, HI 96822, USA

ARTICLE INFO

Available online 30 January 2013

Keywords:
Nitrogen cycle
Biological production
Mesoscale eddies
Submesoscale processes
North Pacific subtropical gyre

ABSTRACT

Vertical profiles of nitrate down to 1000 m depth were obtained about every 5 days and over several years by four profiling floats deployed near Station ALOHA in the North Pacific subtropical gyre. As a first step, we study the episodic and rapid (10–30 days) changes in the depth of constant-nitrate surfaces observed in the float records. These changes are in general correlated with similar changes in the depth of isopycnal surfaces and have a small horizontal scale (horizontal wavelength less than 2°). They are furthermore observed over the whole water column sampled by the floats and throughout the year, with no apparent seasonal cycle. Using these characteristics as well as a 7-year high-resolution time series of potential density at Station ALOHA and a high-resolution numerical simulation of the circulation around the station, we conclude that these episodic changes correspond to the depth anomalies associated with the rapid changes and/or small-scale features of the eddy field. Large vertical velocities associated with submesoscale frontal processes are confined to the surface mixed layer (SML) and play no role in the episodic nitrate events except, perhaps, in late winter to early spring when the SML reaches the top of the nutricline. As a second step, we study the variations of nitrate concentration along isopycnal surfaces, which enables us to isolate the effects of biological processes. In the lower euphotic zone (125–200 m), the nitrate variations reflect the response of the ecosystem to the eddy variability: the shallower the isopycnal surface, the lower the nitrate concentration, and conversely, with nitrate varying in Redfield stoichiometric proportions with oxygen anomaly (defined here as dissolved oxygen minus oxygen saturation). In the upper euphotic zone (0–125 m), in contrast, eddy-induced variations in along-isopycnal oxygen anomaly do not conform with current knowledge about supply and variability of nitrate, ammonium and dissolved organic matter; some other nitrogen source that remains to be identified is required for mass balance.
© 2013 Elsevier Ltd. All rights reserved.

1. Introduction

The eastern North Pacific subtropical ocean is depleted in nutrients in the upper 125 m, yet it sustains new primary productivity at a rate that requires about 143 mmol/m^2 of fixed nitrogen per year (Johnson et al., 2010). Although about 30% of that flux is provided by nitrogen-fixing organisms (Karl et al., 1997), the rest is believed to be sustained by allochthonous nitrate injected by physical processes into the euphotic zone from below. One such mechanism is "eddy pumping" in which mesoscale eddies lift isopycnal and constant-nitrate surfaces into the euphotic zone (McGillicuddy and Robinson, 1997). Estimates of the contribution of this process vary greatly, and other processes may be needed to close the nitrate budget (Falkowski et al., 1991; McGillicuddy et al., 1998, 2003; Oschlies, 2008). One candidate is the large (from ~10 to 100 m/day) vertical velocity associated with submesoscale density fronts (*e.g.* Klein and Lapeyre, 2009; Thomas et al., 2008). From a dynamical point of view, this process differs from the eddy pumping mechanism as it involves *unbalanced* (ageostrophic) and three-dimensional flows while eddies are associated with a *balanced* (geostrophic) and horizontal velocity field. The importance of these large vertical velocities in bringing nutrient into the euphotic zone has been demonstrated mainly in idealized numerical studies; here we used observations in combination with a realistic numerical simulation to assess their role in the North Pacific subtropical gyre.

Four profiling floats have been released at Station ALOHA (158°W, 22°45'N), about 100 km north of Oahu, Hawaii, at different times

* Corresponding author at: University of Hawaii at Manoa, Dept. of Oceanography, 1000 Pope Road, Honolulu, HI 96822, USA. Tel.: +1 808 956 9505; fax: +1 808 956 9225.
E-mail address: fascani@hawaii.edu (F. Ascani).

0967-0645/$ - see front matter © 2013 Elsevier Ltd. All rights reserved.
http://dx.doi.org/10.1016/j.dsr2.2013.01.034

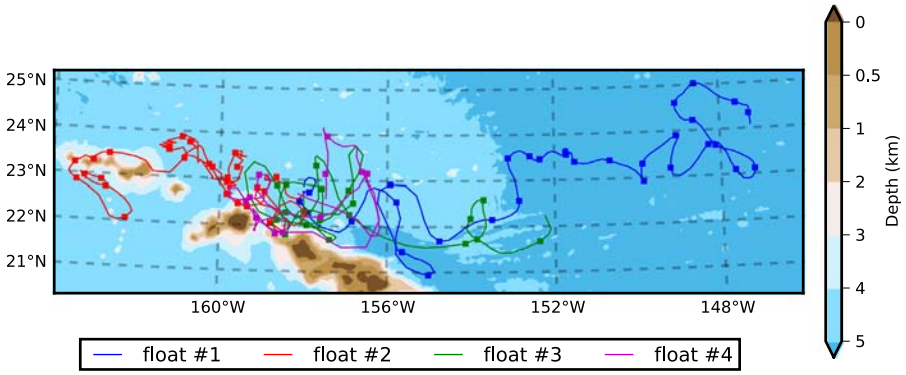


Fig. 1. Trajectories of the four profiling floats released at different times at Station ALOHA (black star). Trajectory of float #1 is shown up to September 2010, when the nitrate sensor failed. Trajectories of floats #2, #3 and #4 are shown up to January 2012. Markers are plotted every 30 days.

since the end of 2007 (Johnson et al., 2010) (Fig. 1). The floats measure profiles of pressure, temperature, conductivity, nitrate and oxygen over the upper 1000 m and about every 5 days. These measurements capture variability on time scales of 30–100 days associated with mesoscale eddies, but shorter events (10–30 days) are also evident (Fig. 2). Johnson et al. (2010) analyzed the data of float #1, in particular the three shallow events of February–April 2009, and concluded that such episodic events could inject up to 88 mmol/m^2/year of nitrate into the euphotic zone. Were this nitrate entirely allochthonous and not locally regenerated, it would represent about 60% of the total nitrogen required to maintain the local new primary production.

To clarify the nature of these episodic events, the float observations of nitrate, oxygen and potential density are analyzed here in conjunction with gridded satellite sea surface height (SSH), a 7-year high-resolution time series of the potential density field from a mooring located at Station ALOHA, the multi-year and near-monthly observations of biological variables made at Station ALOHA as part of the Hawaii Ocean Time-series (HOT) program, and the output from a high-resolution numerical simulation of the circulation around Hawaii.

The observations and the simulation are described in Section 2. In Section 3, we show that the episodic changes in nitrate are largely associated with vertical displacements of isopycnal surfaces and have a small horizontal scale (horizontal wavelength less than 2°). Furthermore, they are found over the whole water column sampled by the floats (upper 1000 m) and throughout the year, with no apparent seasonal cycle. We then evaluate three potential processes to explain the episodic changes: internal waves, the large vertical velocities associated with ageostrophic submesoscale frontal processes, and the anomalies in the depth of isopycnal and constant-nitrate surfaces associated with the rapid changes and/or small-scale aspects of the balanced eddy field. We argue that the latter is the dominant process. Large vertical velocities are confined to the surface mixed layer (SML) which is too shallow to affect the top of the nutricline except occasionally in late winter to early spring when the SML reaches the top of the nutricline.

We continue in Section 4 with a study of the variability of nitrate *along* isopycnal surfaces. We focus primarily on the upper (0–125 m) and lower (125–200 m) euphotic zones and the response of the ecosystem triggered by the eddy variability. A discussion and conclusion follow in Section 5.

2. Observations and numerical simulation

2.1. Float observations

Four Webb Research APEX profiling floats have been released since late 2007 at Station ALOHA: float #1 (5145Hawaii) on December 22, 2007, float #2 (6401 Hawaii) on November 6, 2009, float #3 (6891Hawaii) on May 22, 2010 and float #4 (6403Hawaii) on January 9, 2011 (Fig. 2). Each float measures a vertical profile of pressure, temperature, conductivity, nitrate and dissolved oxygen between the surface and its parking depth of 1000 m about every 5 days. The data are available at www.mbari.org/chemsensor/FloatList.html.

Nitrate and dissolved oxygen data are recorded every 5 m above 100 m, 10 m between 100 and 360 m, and 50 m between 400 and 1000 m. Nitrate concentration is estimated by an *in situ* ultraviolet spectrophotometer (ISUS) with a precision (one standard deviation) of about 0.3 μM and an accuracy of about 0.65 μM (Johnson et al., 2010; Sakamoto et al., 2009). Nitrate data undergo episodic jumps that are corrected following Johnson et al. (2010). Although some negative estimates of nitrate concentrations remain in the corrected dataset, they do not greatly affect the overall results. Dissolved oxygen concentration is estimated by an Aanderaa Optode sensor. The oxygen data have a precision (one standard deviation) of about 1 μM and an accuracy of about 8 μM (Körtzinger et al., 2005). The initial float oxygen estimates, $[O_2]_{float}$, are calibrated via a linear fit to the bottle dissolved oxygen data obtained during the deployment of each float (HOT cruise), excluding regions of steep vertical oxygen gradient. The corrected oxygen float data are then $([O_2]_{float}-a)/b$, where b varies among floats from 0.9462 to 1.009, and a from -4 to -9.9. HOT oxygen data were unavailable for the fourth float at the time of this writing (January 2012), so we use the oxygen data only from the first three floats.

The nitrate sensor of float #1 failed in September 2010 and the data up to this date are used here. The three other floats are still operating and the data up to the time of writing are used.

2.2. Woods Hole Oceanographic Institution-Hawaii Ocean Time-series Station (WHOTS)

WHOTS is a long-term surface mooring at Station ALOHA that has been recording measurements of air–sea fluxes and the upper-ocean response since August 2004 with a high temporal resolution. Information and data are available at www.soest.hawaii.edu/whots/. In this study, we use the temperature and conductivity measurements taken by fifteen Sea-Bird SeaCAT and MicroCAT instruments every 3 min and spaced at 5–20 m in the upper 155 m.

2.3. SSH observations

Maps of absolute dynamic topography are obtained from Archiving, Validation and Interpretation of Satellite Oceanographic (AVISO) data (http://www.aviso.oceanobs.com/). The weekly and gridded "updated" product is used; it is generated using up to four satellites

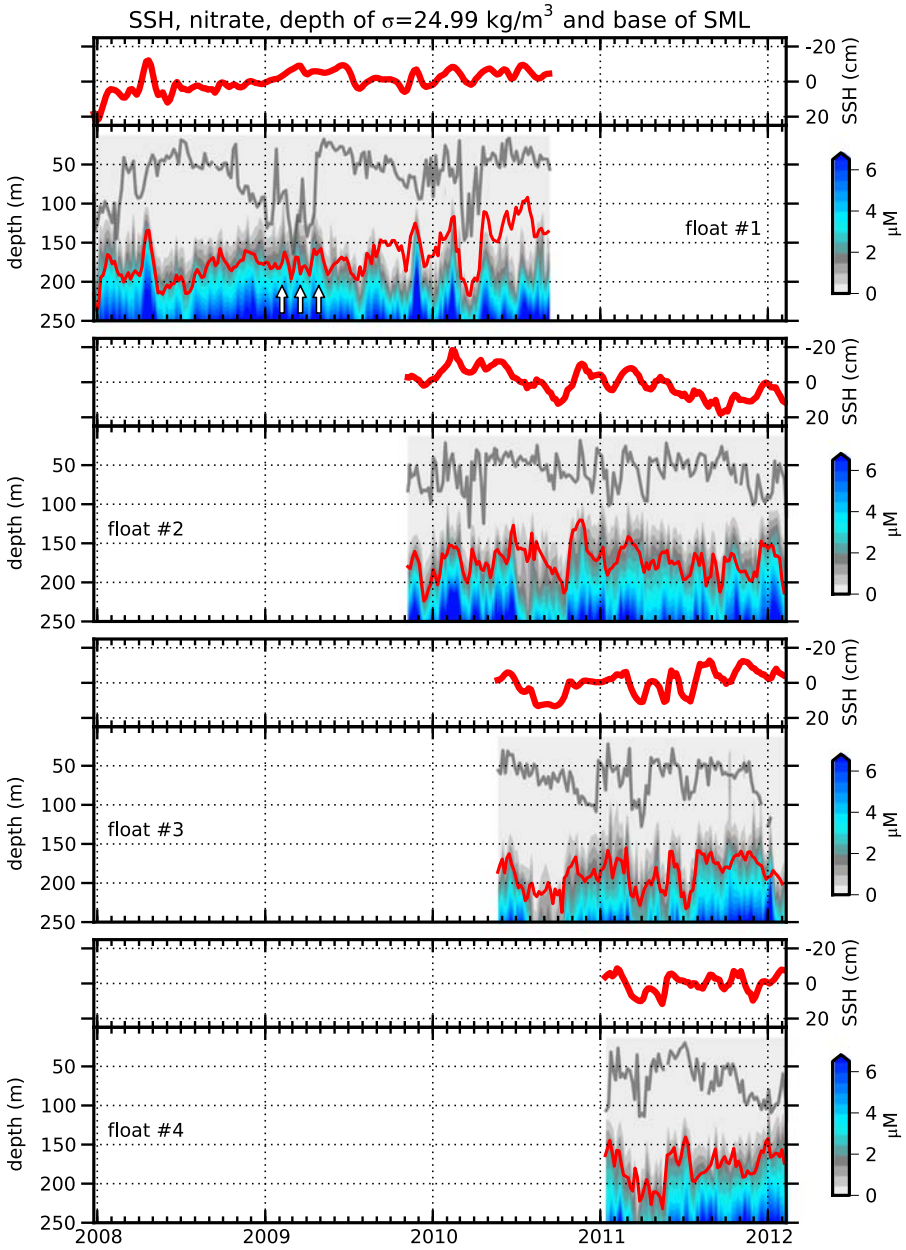


Fig. 2. Nitrate measured by the four profiling floats. The thick red line on the top of each panel is the gridded satellite sea surface height (SSH) along each of the float trajectories, with the *y*-axis inverted. The thin red line inside each panel is the depth of the isopycnal surface $\sigma=24.99$ kg/m^3 that is on average at 175 m. The grey line is the depth of the base of the surface mixed layer (SML), defined here as the depth where the potential density first exceeds the shallowest potential density by 0.125 kg/m^3. The white arrows in the upper panel indicate the three episodic events studied by Johnson et al. (2010). (For interpretation of the references to color in this figure caption, the reader is referred to the web version of this article.)

at a given time and has a nominal resolution of $1/3^\circ \times 1/3^\circ$ although it resolves only features that are at least 2° in wavelength (Chelton et al., 2011). SSH is linearly interpolated in space and time at the location and time of each float profile. It is used here to detect which anomalies in nitrate and stratification are associated with satellite-resolved mesoscale features and which are not.

2.4. HOT data

Several datasets from the HOT program are used: potential density, nitrate plus nitrite concentration and bottle dissolved oxygen concentration from October 1988 to November 2010, as well as dissolved organic nitrogen (DON) and phosphorus (DOP) from October 1988 to January 2001. These data have been collected at Station ALOHA on approximately monthly intervals. Details of the analytical methods and estimates of precision are found in Karl and Lukas (1996), Karl et al. (2001) and the electronic version of the HOT Analytical Methods and Results report (http://hahana.soest.hawaii.edu/hot/methods/results.html). In particular, the precision of DON and DOP measurements are $\pm 7\%$ and $\pm 16\%$, respectively. All the data are downloaded from http://hahana.soest.hawaii.edu/hot/hot-dogs/interface.html.

2.5. Numerical simulation

A numerical simulation of the ocean circulation around Hawaii is also used. The model configuration is described in detail in Jia et al. (2011), but a different surface forcing is used for the present simulation. Briefly, the model is the Hybrid Coordinate Ocean Model (HYCOM), using the Goddard Institute for Space Studies (GISS)

vertical mixing scheme (Canuto et al., 2001; 2002). It is configured with 32 layers in the vertical and a resolution of about 0.04° in longitude and latitude. The horizontal domain extends from 166°W to 150°W and from 16°N to 26°N. The simulation is forced at the surface by the output of a high-resolution (6-km) regional atmospheric model based on the Weather Research and Forecasting Model with initial and boundary conditions from the National Oceanic and Atmospheric Administration (NOAA)/National Centers for Environmental Prediction (NCEP)'s Global Forecast System model (www.nco.ncep.noaa.gov/pmb/products/gfs/; Tu and Chen, 2011). The ocean simulation is forced at its lateral boundaries by the output of the HYCOM Consortium's real-time global ocean prediction system (www.hycom.org). The simulation starts on May 1, 2009 from the state estimate by the global HYCOM simulation and it is currently being updated every month. Daily snapshots of the horizontal velocity and density fields are analyzed; for vertical velocity, the sampling is increased to a snapshot every 3 h.

To compare the simulation to the float profiles and the gridded satellite SSH, two virtual datasets are produced from the output. First, 45 virtual floats are "released" in a region around Station ALOHA (from 160°W to 152°W and from 22.5°N to 24.5°N) on June 1, 2009 and their trajectories are computed until August 2011 using the 1-day snapshots of the horizontal velocity field at 1000 m and a 4th-order Runge–Kutta algorithm. The float initial positions are 1° apart in longitude and 0.5° apart in latitude so that the trajectories can be considered independent. The results do not change qualitatively if we also mimic the surfacing of the real floats by advecting the virtual floats with the surface velocity field for one day at 5-day intervals. The second product is a virtual gridded satellite SSH product. The model SSH output is averaged weekly, then interpolated over the Hawaiian Islands (using a weighted sum of linear interpolations from nearest available points), and finally low-pass filtered in the horizontal using Fourier decomposition to remove features with wavelengths smaller than 2°, the minimum wavelength resolved by the gridded satellite SSH product (Chelton et al., 2011).

Finally, we study the trajectories of virtual water parcels in the simulation by releasing 45 of them along the isopycnal surface $\sigma = 24.99$ kg/m^3, which is on average near 170 m at Station ALOHA. The initial positions of the parcels are the same as for the virtual floats. The parcels stay on the same isopycnal surface and their trajectories are calculated using the horizontal velocity field along that surface. The depth and the vertical component of velocity of the water parcels and isopycnal surfaces are recorded along these trajectories.

3. Nitrate variability due to the vertical displacement of isopycnal surfaces

3.1. Results

Nitrate varies over a range of time scales, from weekly to interannual (Fig. 2). To describe its variability, we introduce the following notation: $d_N(t;d_0)$ and $d(t;d_0)$ are the depth at time t of the

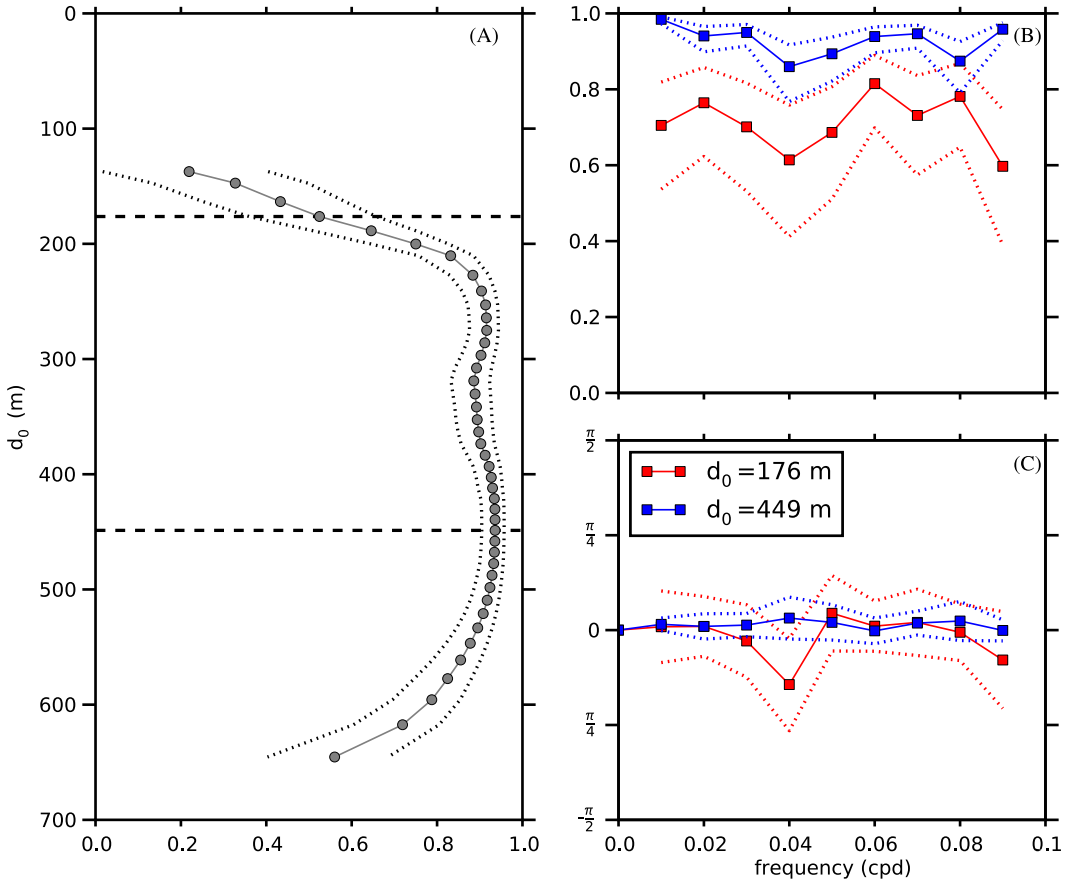


Fig. 3. Correlation between the depth of constant-nitrate and isopycnal surfaces that are on average at the same depth d_0: (a) vertical profile of correlation coefficient, (b) coherence spectrum and (c) phase spectrum for two different averaged depths ($d_0 = 176$ m and $d_0 = 449$ m), indicated by horizontal dashed lines in panel (a). The correlation coefficient is computed using the records of all four floats; the corresponding number of degrees of freedom (*dof*) is 94 for all depths based on the auto-correlation function of $d(t;d_0)$. The coherence and phase spectra are computed from fifty 100-day segments that overlap by 50%, using all four float records (*dof* = 50). In all panels, the dotted lines indicate the 95% confidence interval computed following von Storch and Zwiers (1999). No values are obtained above about 125 m where nitrate concentrations are low and the constant-nitrate surfaces are ill-defined. 'cpd' stands for cycles-per-day.

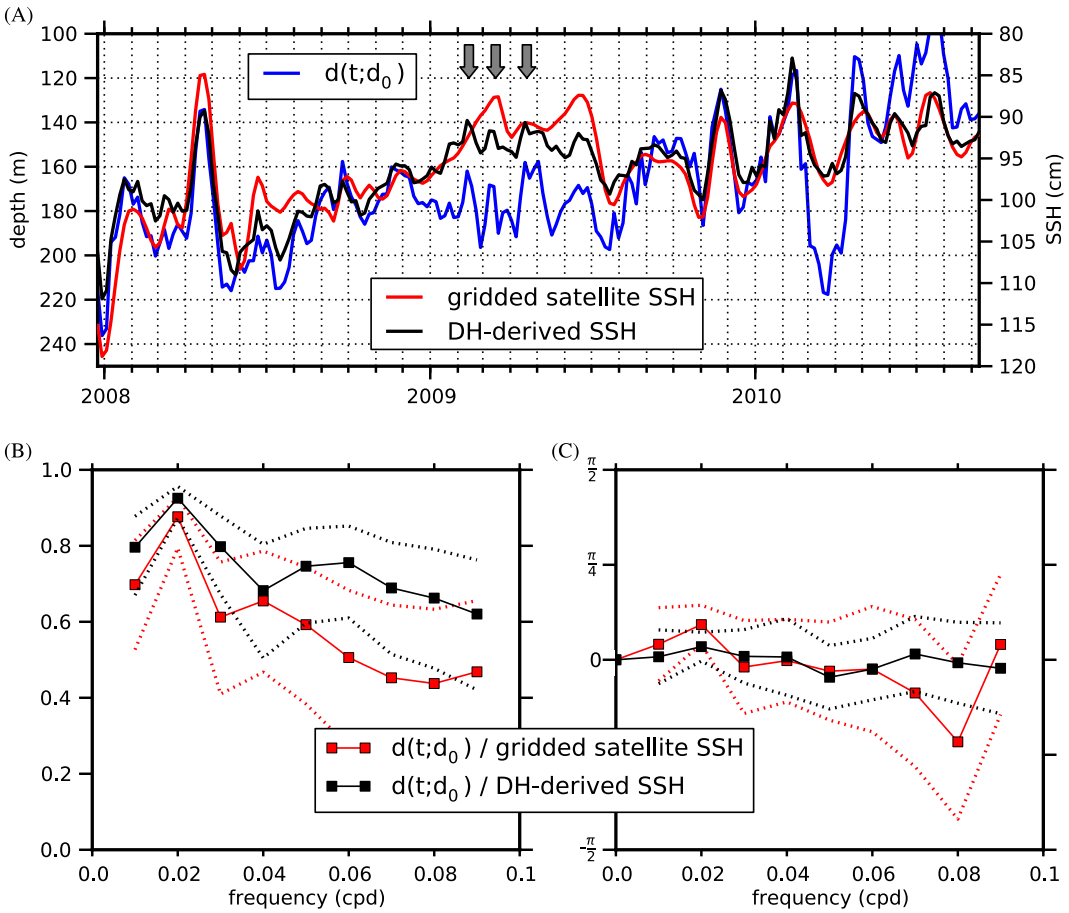


Fig. 4. (a) Time series of $d(t;d_0=176\text{ m})$ (blue; left axis), gridded satellite SSH (red; right axis), and SSH deduced from dynamic height (DH) (black; right axis) from float #1. Notice that the right axis is inverted. DH is computed by vertically integrating the density measured by the floats, and SSH is inferred from DH with a scale factor based on linear regression of satellite SSH on DH. Grey arrows indicate the three episodic events studied by Johnson et al. (2010). (b) and (c) Coherence and phase spectra between $d(t;d_0)$ and gridded satellite SSH (red) and between $d(t;d_0)$ and DH-derived SSH (black). The spectra and their 95% confidence intervals (dotted lines) are computed as explained in the caption of Fig. 3. (For interpretation of the references to color in this figure caption, the reader is referred to the web version of this article.)

constant-nitrate (NO_3^-) and isopycnal (σ) surfaces, respectively that are at the same depth d_0 on average in time over the four float records.

The depth variations of the constant-nitrate surfaces are correlated with depth variations of the isopycnal surfaces (Figs. 2 and 3). The correlation between $d_N(t;d_0)$ and $d(t;d_0)$ increases with depth, reaching 0.9 near 225 m; it stays high down to 550 m and then declines (Fig. 3a). Similar variations of the correlation with depth are obtained when using the multi-year and near-monthly measurements from HOT (Church et al., 2009, their Table 2) and from the Bermuda Atlantic Time-series Study in the North Atlantic subtropical gyre (Siegel et al., 1999, their Fig. 4). Thus, collecting these measurements at a higher resolution in time but over a shorter period, as done here with the floats, does not greatly modify this statistic.

The coherence and phase spectra between $d_N(t;d_0)$ and $d(t;d_0)$ indicate that, within the limits of confidence, the constant-nitrate and isopycnal surfaces are correlated and in phase at all frequencies, with the correlation increasing for all frequencies between the euphotic zone and intermediate depths (Fig. 3b and c). This suggests that most of the nitrate variability at all time scales in the record, including the episodic events, results from vertical advection of isopycnal surfaces on which nitrate is roughly constant.

The episodic events in density and nitrate are associated with features that have an SSH signature not resolved by the gridded satellite SSH. This is shown in Fig. 4. First, the time series of $d(t;d_0=176\text{ m})$ from float #1 is compared to the time series of gridded satellite SSH along the float trajectory (Fig. 4a). It shows that most of the episodic events in $d(t;d_0)$ do not have a signature in gridded satellite SSH. This is the case for instance for the three episodic events studied by Johnson et al. (2010) (arrows in Fig. 4a). This result is confirmed by computing the coherence and phase spectra between $d(t;d_0)$ and gridded satellite SSH (Fig. 4b and c), the coherence generally declines with increasing frequency.

To show that the episodic events in density have nonetheless an SSH signature, we compare $d(t;d_0)$ to the SSH derived from dynamic height (DH). DH is computed by integrating the density field measured by the floats from their parking depth of 1000 m to the surface. Because the motion is weak at 1000 m in this region,[1] DH provides a good estimate of SSH coincident with each profile. Unlike with the gridded satellite SSH, the DH-derived SSH captures most of the episodic events in $d(t;d_0)$ (Fig. 4a), including the three studied by Johnson et al. (2010). This observation is confirmed in the coherence and phase spectra between $d(t;d_0)$ and DH-derived SSH (Fig. 4b and c), the coherence decreases less rapidly with frequency than in the case with gridded satellite SSH, and the two time series are in phase at all frequencies. In consequence, we can conclude that both the episodic nitrate

[1] Using the about 1200-m vertical profile of horizontal velocity taken during HOT cruises since 2003 from shipboard Acoustic Doppler Profiler (SADCP), we find that the mean and mesoscale flow is less than 5 cm/s below 600 m.

and density events are associated with features that have a horizontal wavelength smaller than 2°, the effective horizontal resolution of the gridded satellite SSH product (Chelton et al., 2011).

We next use this scale separation to isolate the episodic nitrate events in $d_N(t;d_0)$, named hereafter $d_N^{epis}(t;d_0)$, from the component of $d_N(t;d_0)$, named hereafter $d_N^{meso}(t;d_0)$, that is spatially and temporally correlated with the gridded satellite SSH. These two components are defined as followed:

$$d_N^{meso}(t;d_0) = \alpha(t;\tau)SSH_{GS}(t)+\beta(t;\tau),$$
$$d_N^{epis}(t;d_0) = d_N(t;d_0)-d_N^{meso}(t;d_0), \quad (1)$$

where SSH_{GS} is the gridded satellite SSH along a float trajectory and α and β are obtained by linearly correlating $d_N(t;d_0)$ and $SSH_{GS}(t)$ over a moving window of length $\tau=90$ days and centered on time t. When the procedure is applied to the time series of float #1, the three episodic events studied by Johnson et al. (2010) (arrows in Fig. 5a and b) stand out clearly in $d_N^{epis}(t;d_0)$. Using a time-limited window instead of the full float time series reduces the effect of gradual changes in background stratification along the float trajectory; we use a window length of 90 days for the typical eddy time scale observed in the region (Chen and Qiu, 2010) but the results depend only weakly on the length of that window. Similar results are also obtained using a running mean.

The standard deviation of $d_N^{epis}(t;d_0)$ is about 10–15 m (Figs. 5 and 6), which is roughly half as large as the standard deviation of $d_N^{meso}(t;d_0)$. The episodic events are found throughout the year with no distinctive seasonality (Fig. 5c). Furthermore,

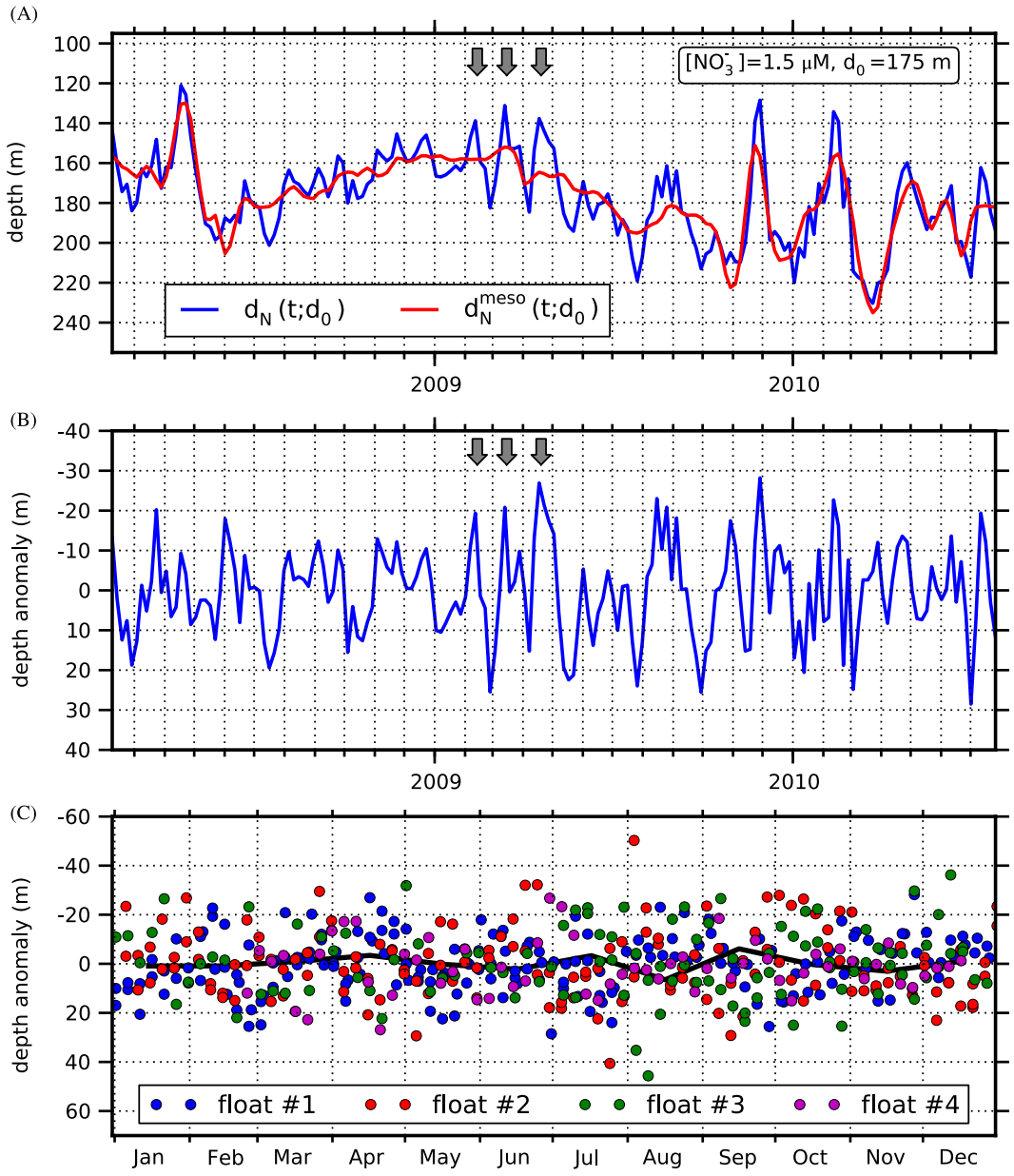


Fig. 5. Temporal behavior of $d_N(t;d_0)$, its mesoscale, $d_N^{meso}(t;d_0)b$, and episodic, $d_N^{epis}(t;d_0)$, components. (a) Time series of $d_N(t;d_0=176$ m) (blue) and $d_N^{meso}(t;d_0)$ (red) (float #1). (b) Time series of $d_N^{epis}(t;d_0)$ defined as the difference between the blue and red curves of (a) (float #1). (c) $d_N^{epis}(t;d_0)$ for all four floats plotted against the month of the year. The thick black line in (c) shows the monthly mean averages. Grey arrows in (a) and (b) indicate the three episodic events studied by Johnson et al. (2010). (For interpretation of the references to color in this figure caption, the reader is referred to the web version of this article.)

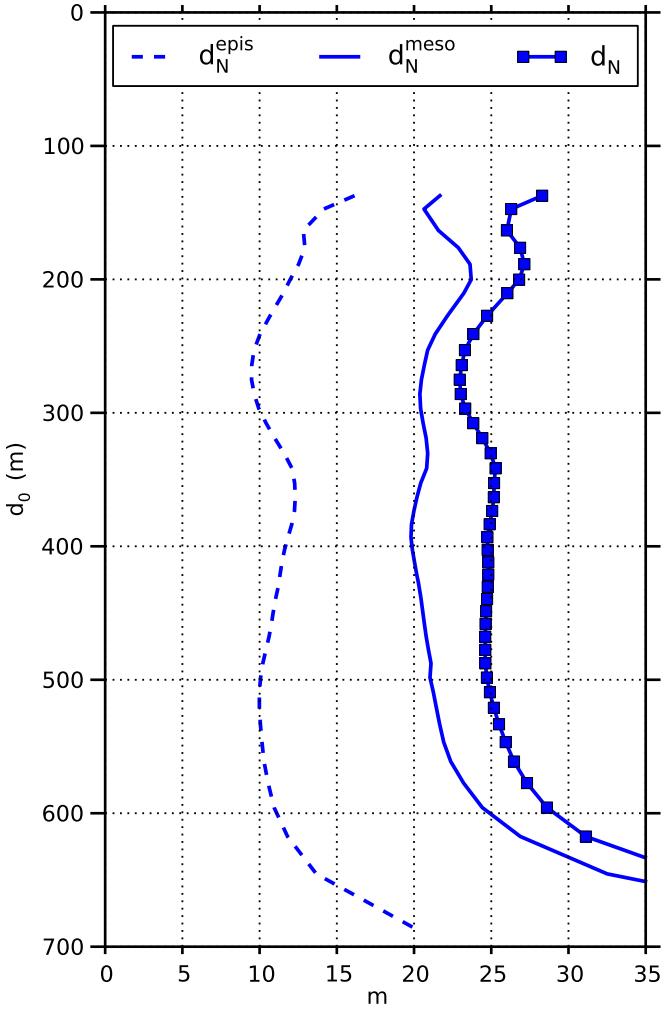


Fig. 6. Standard deviation of $d_N(t;d_0)$, $d_N^{meso}(t;d_0)$ and $d_N^{epis}(t;d_0)$ plotted against the mean depth of each surface of constant-nitrate. No values are obtained above about 125 m where nitrate concentrations are low and the constant-nitrate surfaces are ill-defined.

they are not restricted to the top of the nutricline (upper 200 m) but are found throughout the depth range sampled by the floats. The energy level is lower than that of the mesoscale component, but the variation with depth is similar (Fig. 6). The vertical extent of the mesoscale component is consistent with the generally deep signature of eddies around Station ALOHA (Nolan, 2008).[2] We will see next that these characteristics help to determine the nature of the episodic events.

3.2. What causes the episodic events?

The analysis of the previous section shows that the episodic events in nitrate are associated with anomalies in the depth of both isopycnal and constant-nitrate surfaces that have a small horizontal scale and are found down to at least 1000 m and throughout the year, with no apparent seasonal cycle. Based on these characteristics, we evaluate three possible processes to explain the cause of the episodic events: (1) internal waves, (2) the large vertical velocities associated with the unbalanced flows of submesoscale density fronts and (3) the depth anomalies associated with the rapid changes and/or the small-scale features of the balanced eddy field.

3.2.1. Internal wave field

Internal waves, especially internal tides, raise and lower isopycnal surfaces at frequencies higher than the float sampling rate. Strong internal tides are generated at the nearby Hawaiian Ridge and they propagate northward to the WHOTS mooring at Station ALOHA (*e.g.* Carter et al., 2008; Zhao et al., 2011) (Fig. 7a). The tidal baroclinic energy varies widely, however, over the region sampled by the floats. To see this, we compare the trajectories of the floats in Fig. 1 with published maps of tidal baroclinic energy (Carter et al., 2008, their Fig. 7; Zhao et al., 2011, their Fig. 12). The floats visit regions where the tidal energy is much weaker than at WHOTS. This is the case for the three events studied by Johnson et al. (2010), between 153°W and 152°W and around 23.5°N, well away from the Hawaiian Ridge and the primary beams of internal tide energy.

This conclusion is confirmed by calculating the frequency power spectra of the potential density at 150 m from the 1-hour averaged WHOTS data and the 5-day sampled float time series (Fig. 7a). For frequencies between 0.02 and 0.5 cycles-per-day (cpd), the slopes of the two spectra are the same within confidence intervals; this indicates that the internal tidal energy in the float time series is not as strongly aliased as we would expect if the floats had stayed at Station ALOHA. To confirm this, we compute the averaged frequency power spectrum for the WHOTS time series subsampled at the same frequency as the float time series. In this case, the spectrum is flattened at the high-frequency end (not shown).

If we make the assumption that the internal tides at WHOTS are more energetic than the average sampled by the floats, we can estimate an upper bound for the potential density variance at 150 m in the float time series due to the internal tides. Using the averaged WHOTS frequency power spectrum of Fig. 7a, we calculate the unresolved variance as a function of the Nyquist frequency, the highest frequency resolved by a given sampling, and find that, for a 5-day sampling scheme, at most 20% of the variance can be attributed to the internal tides alone.

3.2.2. Large vertical velocities associated with submesoscale frontal processes

Recently, it has been suggested that large vertical velocities associated with the unbalanced flows of submesoscale frontal processes could contribute to the rapid upward injection of nitrate into the euphotic zone (Lévy, 2008; Lapeyre and Klein, 2006; Lévy et al., 2001, 2012; Mahadevan and Tandon, 2006; Nurser and Zhang, 2000; Spall and Richards, 2000; Thomas et al., 2008). The large values of vertical velocities are, however, confined to the depth range over which the density front exists. In our case, density fronts are limited to the SML, which lies well above the top of the nutricline most of the year (Fig. 2). Only in winter/early spring, can the SML be deep enough for large vertical velocities induced by submesoscale processes to affect the nitrate field.

This qualitative argument is confirmed by the analysis of the numerical simulation. In Appendix, we compare the model to the available observations and discuss its successes and limitations in reproducing the upper ocean variability. Here, we focus on the large vertical velocities associated with submesoscale processes that are generated in the model. Submesoscale flows (identified by large Rossby number R) and their associated large vertical velocity field (w) are found only within the model SML and during the period from January to April (Fig. 8b). In accord with previous numerical studies (Boccaletti et al., 2007), this submesoscale activity results in

[2] We attribute the increase in the standard deviation of $d_N^{meso}(t;d_0)$ and $d_N^{epis}(t;d_0)$ below 550 m to the presence of intermediate water masses at these depths. The origins –and thus initial nitrate content– of these water masses differ more than in the case of the shallower water masses and this causes the nitrate to vary greatly at these depths.

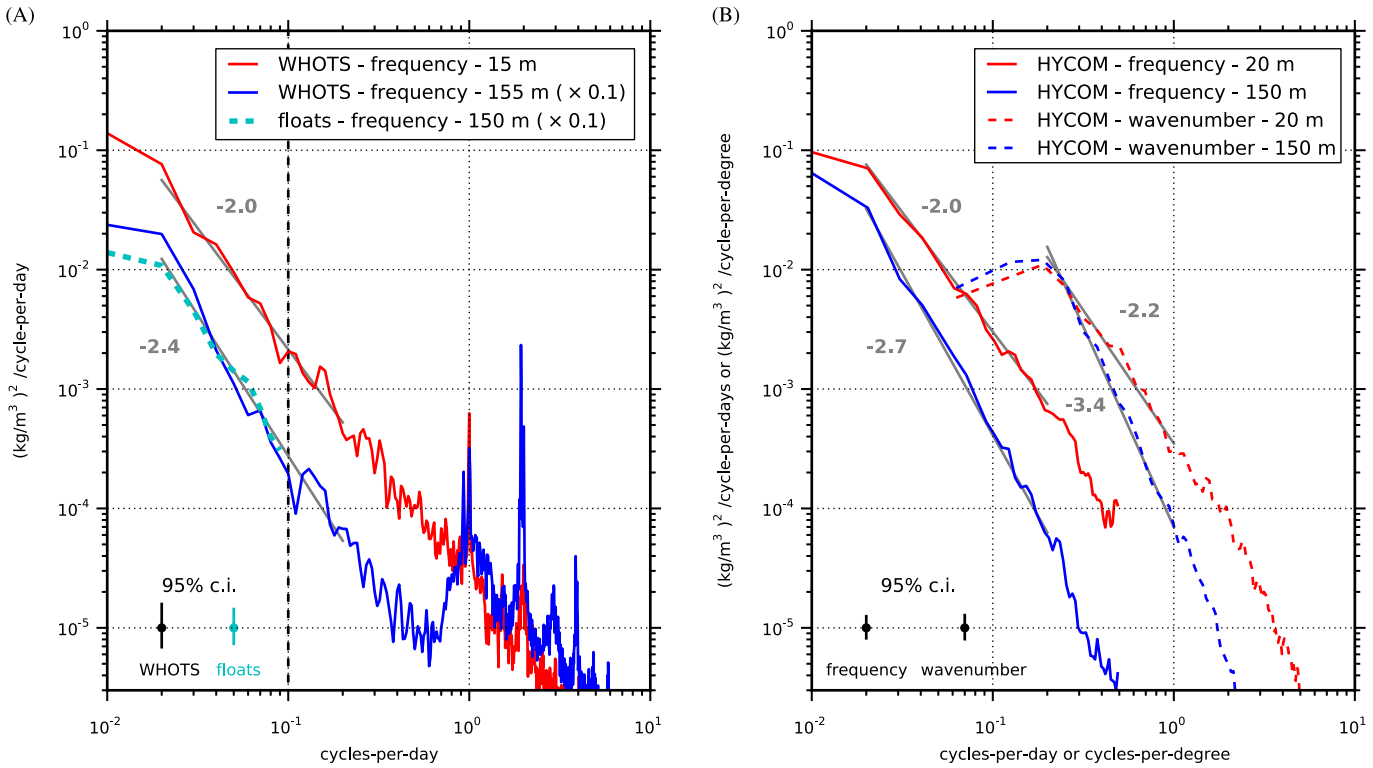


Fig. 7. (a) Averaged *frequency* power spectra of σ from observations: from the 1-hour averaged WHOTS time series (17 non-overlapping 100-day long segments, Hanning window equivalent *dof*=45) at 15 m (plain red) and 155 m (plain blue) and from the 5-day sampled float time series (26 non-overlapping 100-day long segments, Hanning window equivalent *dof*=67) at 150 m (dashed cyan). The three spectra are superimposed to each other for periods longer than 2 days; to help visualize the difference in slope between the two depths, the spectra near 150 m have been multiplied by 0.1 before plotting. (b) Averaged *frequency* and *wavenumber* power spectra of σ from the HYCOM simulation. The frequency spectra are from the 1-day averaged model time series around WHOTS (eight non-overlapping 100-day long segments from eight locations around WHOTS that are at least 2° apart, Hanning window equivalent *dof*=171) at 20 m (plain red) and 150 m (plain blue). The wavenumber spectra are from two zonal sections (22.5°N and 24.5°N; 54 segments of 16° length taken once every 30 days, Hanning window equivalent *dof*=144) at 20 m (dashed red) and 150 m (dashed blue). Each temporal or spatial segment has been detrended in time or space and a Hanning window is applied to each of them before performing the Fourier decomposition. The 95% confidence intervals are shown with vertical bars and computed as described in von Storch and Zwiers (1999). Grey lines and numbers indicate the slope of each spectrum calculated by least-square fits between 5 and 50 days for frequency spectra and 1° and 5° for wavenumber spectra. The vertical dashed line in (a) indicates the Nyquist frequency for the float sampling interval. (For interpretation of the references to color in this figure caption, the reader is referred to the web version of this article.)

a restratification of the SML seen in Fig. 8b by a shoaling of the base of the SML whenever the Rossby number or w is large. As concluded above, only during late winter and early spring, could we thus expect the large vertical velocities associated with the submesoscale activity to affect the top of the nutricline.

3.2.3. *Rapid changes and small-scale aspects of the balanced eddy field*

Given the spatial and temporal characteristics of the episodic nitrate events found in the previous section, another candidate for the events is the depth anomalies in isopycnal and constant-nitrate surfaces associated with the evolving and convoluted eddy field. Individual eddies can vary rapidly (over a period of one to two weeks) in shape and amplitude because of their interaction with other eddies. The rapid changes and small-scale features of the balanced eddy field would not be well resolved by the gridded satellite SSH; more importantly, they would appear as episodic events in the depth of isopycnal and constant-nitrate surfaces in a float time series over a large portion of the water column and with no apparent seasonality, consistent with the observed characteristics of the episodic events.

Assuming that the spatio-temporal structure of the density field in the model is representative of the ocean's one, we use the numerical simulation to explore this hypothesis. As in the float observations, we find episodic events in the model potential density time series along the trajectories of virtual floats that are not resolved by a virtual product of gridded satellite SSH. Among the 45 virtual float time series, we find two types of situations in which these episodic anomalies appear. The most common case occurs when a float is sampling the sharp edge of a rapidly evolving eddy. An example is shown in Fig. 9. The less frequent case is the occurrence of shallow or deep isopycnal surfaces inside a submesoscale filament of density (Fig. 10). Shallow and cold filaments are found particularly during the winter-to-spring transition, as discussed previously.

All these arguments thus support the conclusion that the primary cause for the episodic anomalies in the depth of constant-nitrate surfaces in the float time series is the floats sampling the rapidly evolving balanced eddy field and/or its small-scale features. Although some of the small-scale features may be submesoscale, they are associated with a nearly balanced horizontal flow and do not involve large vertical velocities.

4. Nitrate variability along isopycnal surfaces

Nitrate also varies because of biological processes. To isolate this portion of the variability from the variability associated with the vertical displacements of isopycnal surfaces, we study the changes of nitrate along isopycnal surfaces. To help interpret the observations, we also study the variations of oxygen anomaly

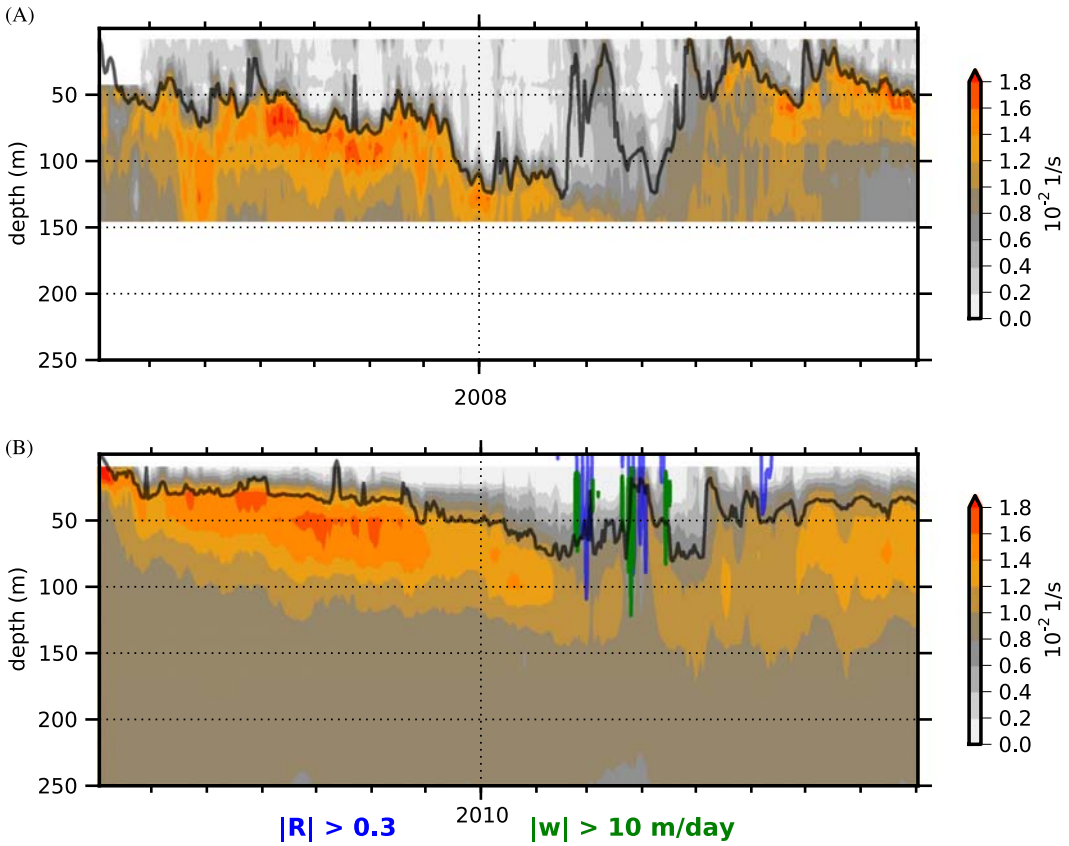


Fig. 8. Buoyancy frequency (a) at the WHOTS mooring (1-day averages) and (b) in HYCOM at the WHOTS location (1-day running mean). Notice that the time is different between the two panels. These particular periods were chosen for their similar spring restratification events; this is because, although restratification is widespread in the simulation, it does not necessarily occur at each point every year. In both panels the black line shows the base of the SML. In (b) the blue contours show where the Rossby number R is larger than 0.3 and the green contours show where the 1-day averaged vertical component of velocity, w, is larger than 10 m/day. (For interpretation of the references to color in this figure caption, the reader is referred to the web version of this article.)

(defined as dissolved oxygen minus oxygen saturation) along the same surfaces.

In Fig. 11 are plotted the along-isopycnal nitrate, $[NO_3^-](\sigma)$ (left column), and the along-isopycnal oxygen anomaly, $[O_2]_{ano}(\sigma)$ (middle column), against the depth of the isopycnal surface. This is done for three surfaces, one that is within the upper euphotic zone (0–125 m), one that is within the lower euphotic zone (125–200 m) and one that is always in the aphotic zone (>200 m). Additionally (Fig. 11, right column), to study if any of the variations are in the stoichiometric proportions predicted by Redfield et al. (1963), $[NO_3^-](\sigma)$ is plotted against $[O_2]_{ano}(\sigma)/R$ where $R=-10.5$ is the corrected Redfield ratio of oxygen production to nitrate uptake (Anderson, 1995).

We find three regimes. The first regime is found whenever the isopycnal surface is within the upper euphotic zone; there, nitrate concentrations are always low (<1 μM) while anomalies in oxygen concentrations vary by as much as 30 μM in such a way that the shallower the isopycnal surface, the larger the oxygen anomaly (Fig. 11a and b). In Fig. 11c, we see these oxygen changes are not associated with changes in nitrate concentration expected from Redfield stoichiometry (represented by a dashed line in the right panels of Fig. 11). This regime has already been noticed by Johnson et al. (2010) based on the *seasonal* variability of oxygen anomaly and the present results indicate that the regime is also observed over the spatial and temporal scale of eddies.

The second regime is found whenever the isopycnal surface is within the lower euphotic zone; unlike in the first regime, nitrate and oxygen anomaly concentrations vary in concert (by as much as 2 μM for nitrate and 20 μM for oxygen anomaly) following an inverse relationship that satisfies the Redfield prediction (Fig. 11; middle panels). The relationships are such that the deeper the surface, the larger $[NO_3^-](\sigma)$, and the lower $[O_2]_{ano}(\sigma)$. This suggests that, in this regime, when the isopycnal surface shallows, oxygen is produced and nitrate is consumed in Redfield proportions, and conversely.

The third regime is found whenever the isopycnal surface is within the aphotic zone. In this case, oxygen anomaly and nitrate on an isopycnal surface are not correlated with its variations in depth, but they still co-vary in Redfield proportions (Fig. 11, lower panels).

The linear relationships between either nitrate or oxygen anomaly concentration on an isopycnal surface and the depth variations of that surface are found only within the euphotic zone. This is confirmed by the vertical profiles of the fraction of variance of $[NO_3^-](\sigma)$ and $[O_2]_{ano}(\sigma)$ fit by a linear dependence on the depth of the isopycnal surface (Fig. 12a). Both fractions peak within the lower euphotic zone with a maximum of about 10% for nitrate and 60% for oxygen anomaly. The fact that the peak for $[O_2]_{ano}(\sigma)$ is shallower than the peak for $[NO_3^-](\sigma)$ is a consequence of the different behavior of nitrate and oxygen anomaly between the first two regimes. In any case, these characteristics suggest that the relationships arise from light-dependent biological processes and are the signature of the ecosystem response to eddy-induced vertical displacements. In the aphotic zone (third regime), there is not enough light for the ecosystem to react to these vertical displacements, explaining the lack of correlation between the nitrate and oxygen anomaly concentrations along isopycnal

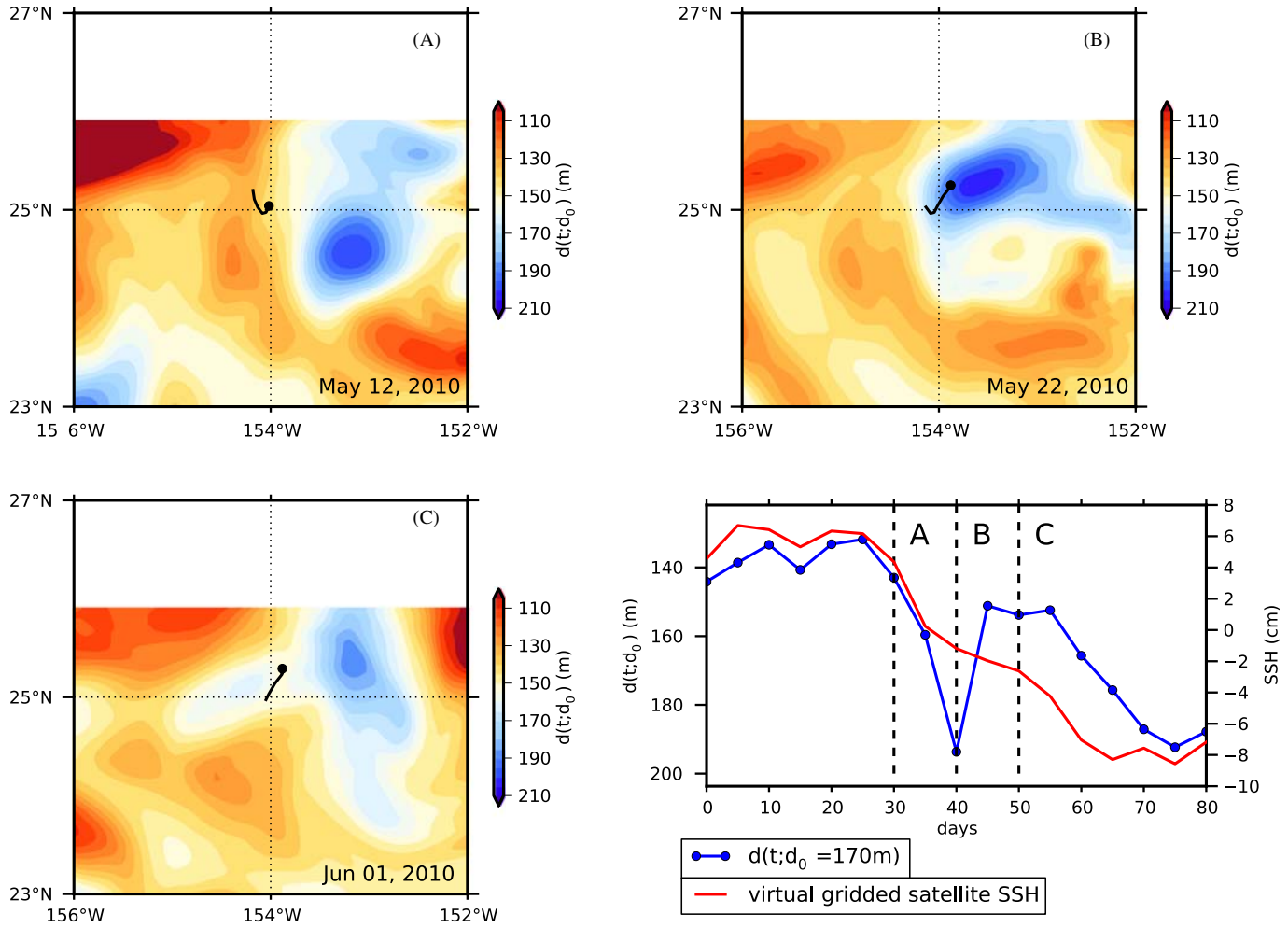


Fig. 9. Example of a virtual float record from the numerical simulation. Because the eddy evolves rapidly over the time period and because its sharp edge is smoothed in the virtual gridded satellite SSH, this leads to an episodic event in the virtual float time series of the depth of an isopycnal surface. The panels titled A, B and C are the maps of the depth of the isopycnal surface $d(t;d_0=175\ \mathrm{m})$ for $\sigma=24.99\ \mathrm{kg/m^3}$ at 10-day intervals. The position of the float at the time of the map is indicated by a black dot, with a tail for its trajectory over the last 25 days. The lower right panel shows the time series of the depth of the isopycnal surface (blue) and the time series of the virtual satellite gridded SSH (red) along the virtual float trajectory. The times of the three maps are marked by vertical dashed lines. (For interpretation of the references to color in this figure caption, the reader is referred to the web version of this article.)

surfaces and the depth of these surfaces; the Redfield co-variation in nitrate and oxygen anomaly observed at these depths reflects instead the different origins of the water masses.

Similar profiles of variance are found when we perform the calculation using the potential density, nitrate plus nitrite, and bottle dissolved oxygen data from the HOT program (Fig. 12a). The main difference between the float and HOT data is that more variance of float oxygen (about 60%) than of HOT oxygen (about 30%) is explained by a linear relationship with the depth of the isopycnal surface. Although this difference is statistically significant, we have not identified the reason for it: interannual variability in the HOT dataset, the presence of extreme oxygen values, and the fact that not all float data are independent, have each been ruled out as possible explanations. Despite this caveat, the similarity of the profiles obtained from the two different datasets suggests that the linear relationships found here are robust and are not sensitive to the spatial and temporal sampling of the data.

A question remains concerning the variability in oxygen anomaly observed in the first regime: how can it be maintained given that nitrate concentration is always too low to sustain it? A likely answer is that a source of nitrogen other than nitrate is responsible for these oxygen variations but the difficulty is to identify the source. The two main alternative sources of nitrogen, ammonium and DON, are inadequate for different reasons. The pool of ammonium is simply too small (less than 0.03 μM; Karl et al., 2008; Sutka et al., 2004). The DON pool is large enough and varies over a range that could explain the oxygen variations (between 4 and 8 μM above 125 m; Karl et al., 2001); but, if DON were responsible for the oxygen variations, along-isopycnal DON concentration should vary with the depth of the isopycnal surface, just as nitrate concentration does in the second regime. This does not appear to be the case, however, and the same is true for DOP (Fig. 12b). We also do not find any statistically significant correlation between DON (or DOP) and oxygen anomaly (not shown). Thus we are ruling out ammonium and DON as the cause of the oxygen variations in the upper euphotic zone. These conclusions are based on the eddy variability of oxygen anomaly but they confirm similar conclusions drawn from the seasonal variability of inorganic carbon (Karl et al., 2003) and oxygen anomaly (Johnson et al., 2010).

5. Discussion and conclusion

In this study, we analyzed the depth anomalies of constant-nitrate and isopycnal surfaces measured every 5 days and over several years

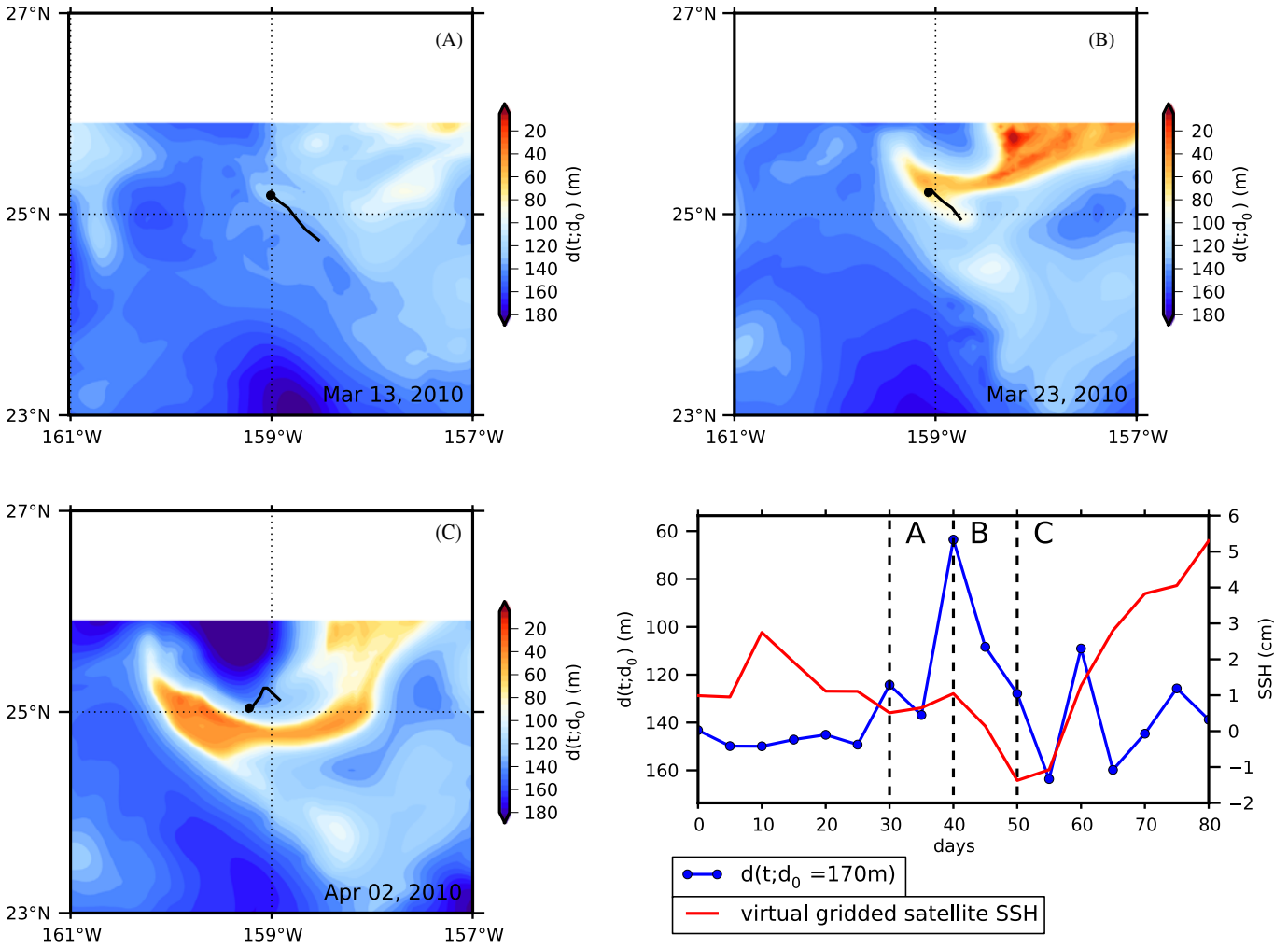


Fig. 10. Example in the numerical simulation of a virtual float sampling a shallow filament of cold water. The filament has no signature in the virtual satellite gridded SSH, but appears as an episodic event in the time series of the depth of an isopycnal surface along the virtual float trajectory. The panels are arranged as in Fig. 9.

by profiling floats released at Station ALOHA in the North Pacific subtropical gyre. In an early subset of this data, Johnson et al. (2010) noticed episodic shallow nitrate anomalies that could provide enough nutrient to the euphotic zone to maintain, together with other processes, the observed new primary production.

The present analysis shows that these episodic anomalies are generally correlated with changes in the depth of isopycnal surfaces, are associated with features of relatively small horizontal scale and are found throughout the water column and the year, with no apparent seasonality. Using these characteristics in combination with observations of the density field and a numerical simulation, we conclude that the events are principally due to the floats sampling the rapid changes and/or small-scale features of the balanced eddy field and their associated depth anomalies in isopycnal and constant-nitrate surfaces. Although we find large vertical velocities associated with submesoscale density fronts in the model SML, they can affect the depth of the nutricline only during late winter to early spring when the bottom of the SML reaches the top of the nutricline. Whether they do affect the nutrient input into the euphotic during this time of the year has yet to be determined, however; a dedicated observational program focusing on this period of the year would be needed for this purpose.

This work calls for caution in applying to the North Pacific subtropical ocean the results of idealized numerical studies concerning the effect of frontal submesoscale processes on the depth of the nutricline. The key factor is the position of the nutricline with respect to density fronts. To our knowledge, in all numerical studies that show the importance of submesoscale processes, the nutricline initially *crosses* the density front (Lévy, 2008; Lapeyre and Klein, 2006; Lévy et al., 2001; Nurser and Zhang, 2000; Spall and Richards, 2000; Thomas et al., 2008). This is a valid configuration for the strong and deep density fronts observed along the Kuroshio Extension and the Gulf Stream, but it is not applicable to the fronts near Station ALOHA. There, the fronts are limited to the SML, which is usually well above the top of the nutricline.

Nitrate also varies because of biological processes. To study this portion of the variability and to help to interpret it, we study the variations of nitrate and oxygen anomalies along isopycnal surfaces. We find three regimes. Within the upper euphotic zone, nitrate concentrations are near zero while oxygen anomalies are higher when the isopycnal surface shoals, and lower when it deepens. Within the lower euphotic zone, oxygen anomalies vary in a similar fashion as in the first regime but its variations are now correlated with nitrate variations in agreement with Redfield stoichiometry. Within the aphotic zone, nitrate and oxygen anomaly variations on an isopycnal surface are uncorrelated with depth variations of that surface, but they still co-vary in Redfield proportions.

The lower euphotic zone regime can be interpreted as the ecosystem response to eddy variability. For this, the study of

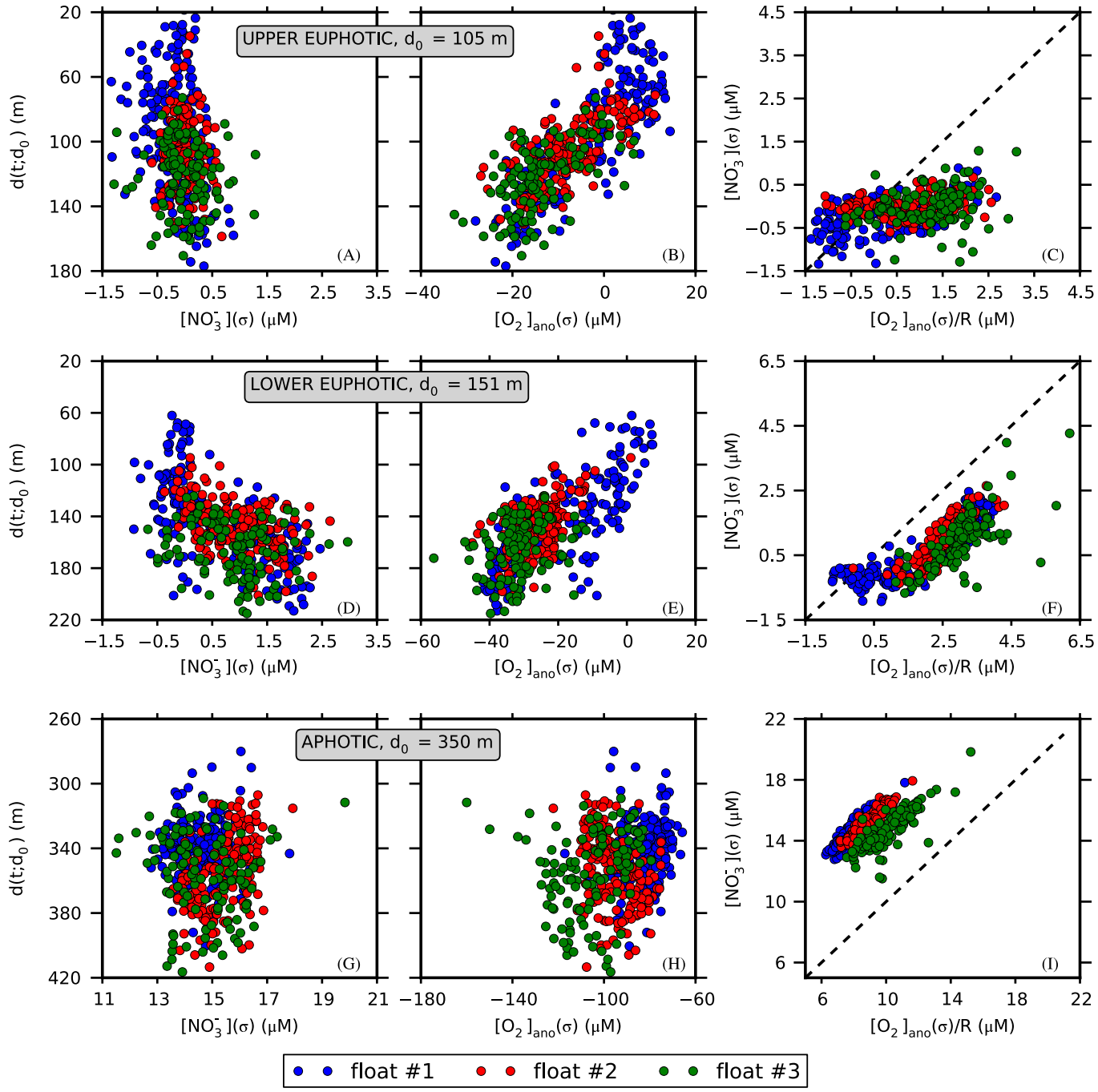


Fig. 11. (left column) Along-isopycnal nitrate versus depth of isopycnal surface. (middle column) Along-isopycnal oxygen anomaly versus depth of isopycnal surface. (right column) Along-isopycnal oxygen anomaly (scaled by the modified Redfield ratio $R=-10.5$ of oxygen production to nitrate uptake) versus along-isopycnal nitrate. In the right panels, the slope of the dashed line indicates variations that are in Redfield stoichiometric proportions. (upper row) Along the isopycnal surface $\sigma=24.35$ kg/m^3 that is on average within the upper euphotic zone ($d_0=105$ m). (middle row) Along the isopycnal surface $\sigma=24.8$ kg/m^3 that is on average within the lower euphotic zone ($d_0=151$ m). (lower row) Along the isopycnal surface $\sigma=26.15$ kg/m^3 that is on average within the aphotic zone ($d_0=350$ m). Only the data from the first three floats are used in this plot because the corrected oxygen data for the fourth float were not available at the time of writing. (a) $[NO_3^-](\sigma)$ versus $d(t;d_0)$, (b) $[O_2]_{ano}(\sigma)$ versus $d(t;d_0)$, (c) $[O_2]_{ano}(\sigma)/R$ versus $[NO_3^-](\sigma)$, (d) $[NO_3^-](\sigma)$ versus $d(t;d_0)$, (e) $[O_2]_{ano}(\sigma)$ versus $d(t;d_0)$, (f) $[O_2]_{ano}(\sigma)/R$ versus $[NO_3^-](\sigma)$, (g) $[NO_3^-](\sigma)$ versus $d(t;d_0)$, (h) $[O_2]_{ano}(\sigma)$ versus $d(t;d_0)$ and (i) $[O_2]_{ano}(\sigma)/R$ versus $[NO_3^-](\sigma)$.

Martin and Pondaven (2003), which differentiates the response of the ecosystem depending on the type of eddies involved (either linear Rossby waves or nonlinear coherent structures), provides a useful framework. They note that in the small-amplitude limit, eddies become linear Rossby waves, which lift parcels in the pycnocline up and down as they pass but which produce no net horizontal displacement. With sufficiently large amplitude, however, eddies are nonlinear coherent structures that can trap water parcels, transporting them laterally with the eddy over large distances with little vertical motion. Although these limiting cases imply very different time histories of nitrate following a water parcel, both cases, or anything in between, can yield the observed linear relationships between the depth of an isopycnal surface and the concentration of either nitrate or oxygen anomaly along that surface. In the small-amplitude limit, nitrate concentration on an isopycnal surface decreases as the surface rises

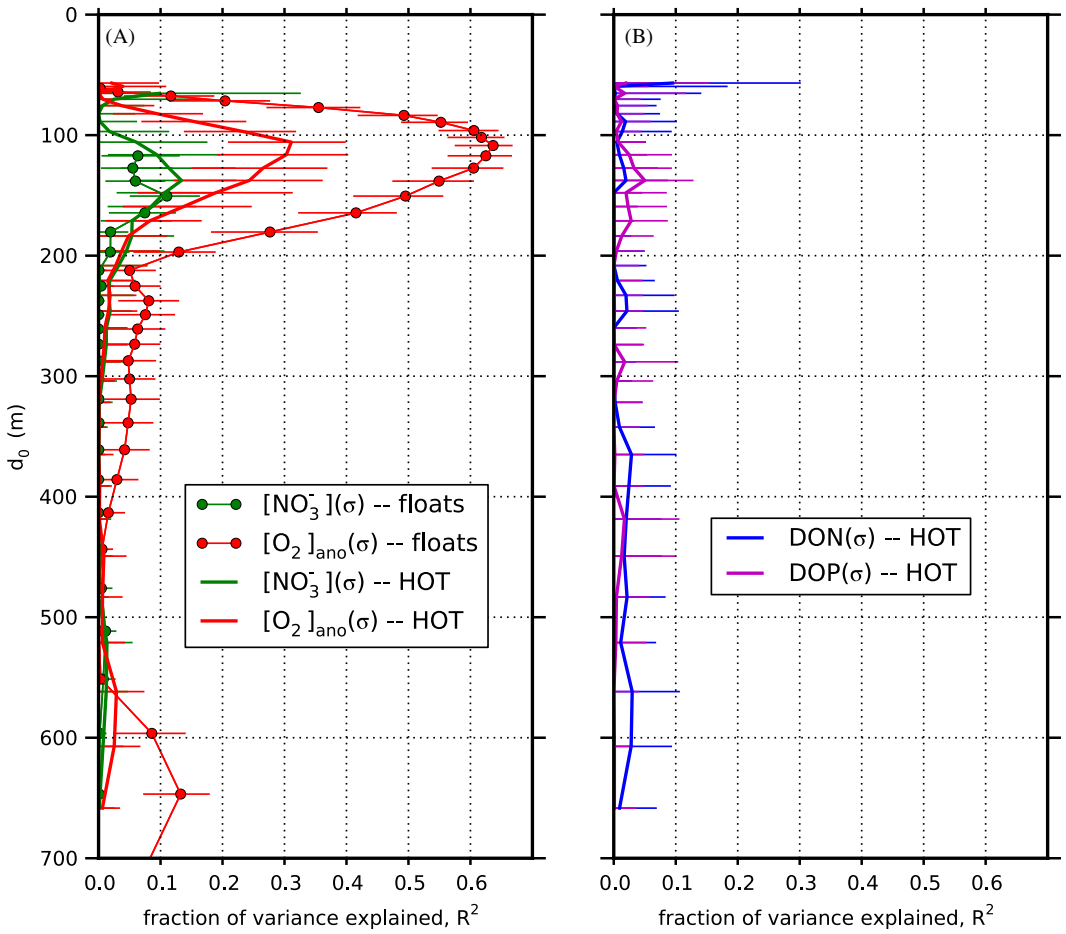


Fig. 12. Fraction of variance of $[NO_3^-](\sigma)$ (green), $[O_2]_{ano}(\sigma)$ (red), dissolved organic nitrogen (DON; blue) and dissolved organic phosphorus (DOP; magenta) explained by a linear dependence on the depth of the isopycnal surface. The fraction is plotted against the mean depth of each isopycnal surface. Lines with markers indicate data from the floats while plain lines indicate data from the HOT program. For the HOT data, $[NO_3^-](\sigma)$ represents nitrate plus nitrite. Only the data from the first three floats are used. Nitrate results are plotted only when at least 20% of the data along an isopycnal surface exceed 0.25 μM. For the other quantities, values are missing near the surface where isopycnal surfaces are always ill defined. Horizontal bars correspond to the 95% confidence intervals calculated using a bootstrapping resampling technique (1000 realizations). (For interpretation of the references to color in this figure caption, the reader is referred to the web version of this article.)

above its mean level, and the increased light powers more rapid photosynthesis; conversely, nitrate concentration increases as the surface drops below its mean level because respiration plus diffusive flux convergence recharge it faster than it is consumed by photosynthesis. If this net nitrate response to varying light levels occurs on time scales similar to or shorter than those of the vertical motion, then the observed depth-nitrate correlation results. When the eddies are coherent structures, however, the nitrate concentration of a given parcel equilibrates with its new depth within the eddy. Parcels on a given isopycnal surface in anticyclonic eddies are deeper than those in cyclonic eddies, so they equilibrate at higher nitrogen levels, leading again to a correlation between depth and nitrate concentration when sampling an ensemble of eddies.

The present float observations do not tell us the degree to which water parcels in the lower euphotic zone are trapped and transported by eddies, so we turn to the numerical simulation. To give an idea of the trajectories of water parcels, we "release" 45 virtual parcels in the numerical simulation along the isopycnal surface $\sigma = 24.99\ \mathrm{kg/m^3}$ (which is on average at about 170 m depth at Station ALOHA). We find that all of the parcels move in the vertical over dozens of meters (Fig. 13a), largely in concert with the vertical motions of the isopycnal surface (Fig. 13b). Visual inspection of the parcel trajectories relative to the eddies as seen in the model SSH indicates that most of the parcels do not track mesoscale structures. We conclude that in the model, the mesoscale energy near Station ALOHA is closer to the linear Rossby wave regime than to the nonlinear eddy regime. The actual degree and duration of parcel trapping in the ocean, however, remain to be determined. In any case, the observations are qualitatively consistent with both a scenario where parcels move only in the vertical by linear Rossby waves and a scenario where parcels are stationary in the vertical but moved horizontally being trapped inside a coherent eddy.

Concerning the upper euphotic zone, we have shown that the oxygen anomaly variations in the absence of matching variability in measured nitrate described by Johnson et al. (2010) at the seasonal time scale also prevail at the eddy time scale. These variations remain, however, puzzling. Confirming prior conclusions based on the seasonal variability of inorganic carbon (Karl et al., 2003) and oxygen anomaly (Johnson et al., 2010), we exclude ammonium and DON as alternative sources of nitrogen based on their co-variability with oxygen at the eddy time scale. Another candidate is intra-cellular nitrogen transported by vertically migrating phytoplankton (*e.g.* Johnson et al., 2010; Letelier and Karl, 1998; Singler and Villareal, 2005) but quantifying this vertical nitrogen flux on a regular basis will be challenging and remains to be done.

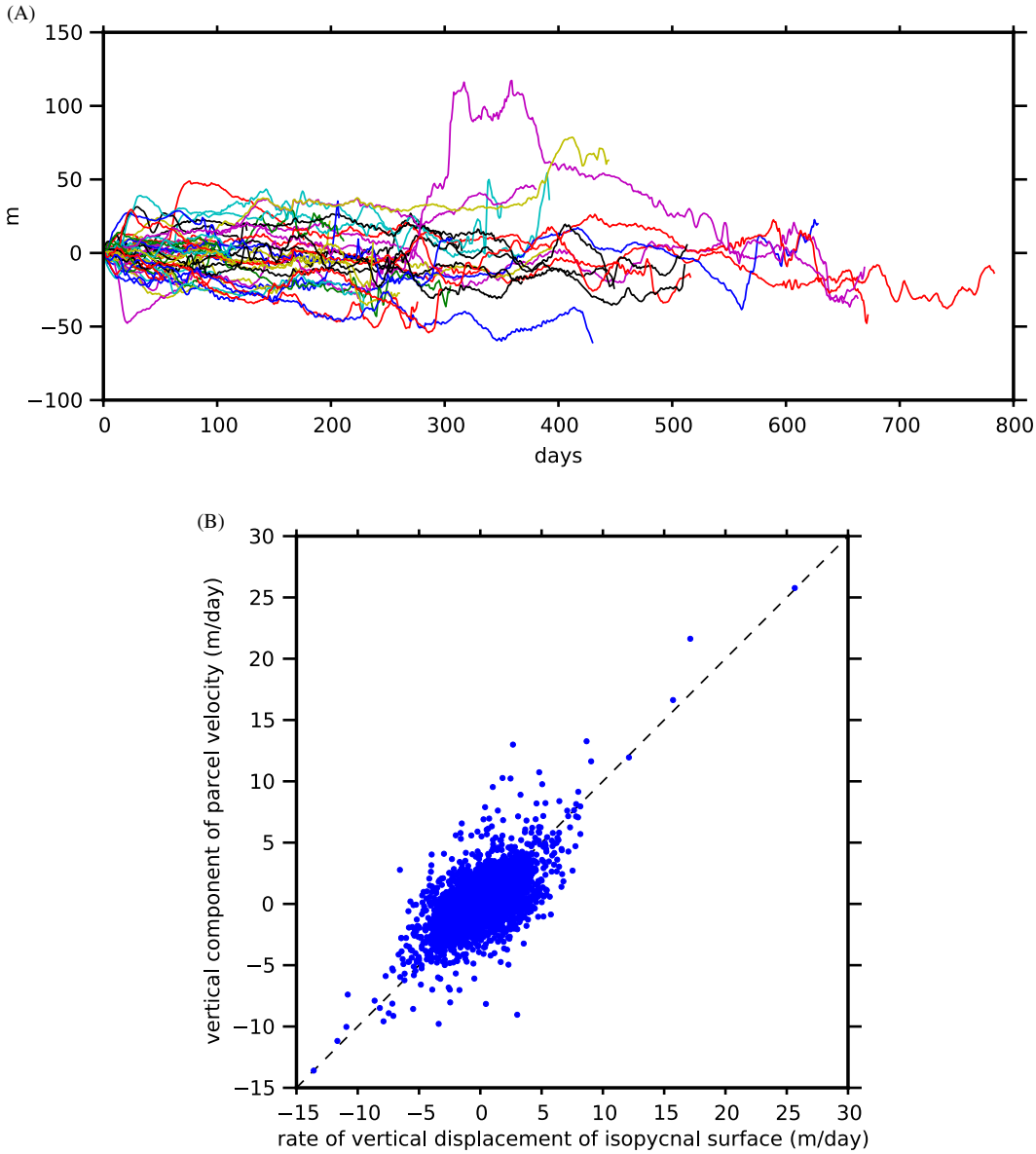


Fig. 13. (a) Time series of the depth of all 45 virtual water parcels "released" in the numerical simulation along the isopycnal surface $\sigma=24.99$ kg/m^3 ($d_0=175$ m). The initial depth of each parcel has been removed. The length of the time series depends on the time each parcel stays in the domain without hitting an island. (b) Vertical component of parcel velocity versus the rate of vertical displacement of the isopycnal surface. The dashed line indicates the one-to-one relationship.

Acknowledgments

We would like to thank Paulo H.R. Calil, John R. Casey and Lionel Guidi for valuable discussions, two anonymous reviewers who helped to clarify the manuscript, as well as Fernando E. Santiago-Mandujano for processing and making available the WHOTS data. The acquisition and development of the floats were funded through a grant of the National Science Foundation (NSF; OCE-0825348) awarded to Kenneth S. Johnson and Stephen C. Riser. WHOTS is funded by the National Oceanic and Atmospheric Administration (NOAA) Climate Observation Division through grant NA09OAR4320129 to the Cooperative Institute for the North Atlantic Region at the Woods Hole Oceanographic Institution and by NSF as part of the Hawaii Ocean Time-series (grants OCE-0327513, OCE-752606, and OCE-0926766). David Karl is supported by the Center for Microbial Oceanography: Research and Education (C-MORE) through NSF grant EF-0424599 and by the Gordon and Betty Moore Foundation. This research was supported by the Japan Agency for Marine-Earth Science and Technology (JAMSTEC), by the National Aeronautics and Space Administration (NASA) through grant NNX07AG53G and by NOAA through grant NA11NMF4320128FA, which sponsor research at the International Pacific Research Center (IPRC). Financial support was also provided by C-MORE. All figures are produced with matplotlib, a freely available python-based plotting software (matplotlib.org). IPRC contribution #944 , C-MORE contribution #379 and SOEST contribution #8849.

Appendix. Assessment of the model submesoscale activity

To assess whether the model simulates the submesoscale activity with a useful degree of realism, we here compare the model to observations. There are some notable differences. Compared to the WHOTS observations, the model SML is shallower and the transition between the SML and the seasonal thermocline is smoother (Fig. 8). Furthermore, using empirical orthogonal function (EOF) analysis of the potential density field from the model and HOT data, we find that the first EOF

(representing about 70% and 60% of the variance in the model and in HOT, respectively) decays with depth much faster in the model than in the observations. Consequently, at 150 m the amplitude of potential density variability is lower in the model than in the observations by a factor of about 1/3; this is seen in Fig. 7 where the frequency power spectra at 150 m from WHOTS and the floats *multiplied* by 0.1 have the same level as the model frequency power spectrum.

Despite these limitations, the model reproduces several aspects of upper ocean structure relevant to this study. First, the seasonal cycle includes a well defined SML sitting on top of a deepening seasonal thermocline from May to December and a SML of varying thickness on top of an eroded seasonal thermocline from January to April (Fig. 8). Second, the temporary shoaling of the base of the SML observed sometimes in spring at WHOTS (Fig. 8a) may be indicative of the restratifying events that are the main signature of the submesoscale activity in the model. Finally, the model reproduces strong frontal features during spring similar to those reported from the vicinity of Station ALOHA (Letelier et al., 2000). As in the analysis of remote sensing imagery by Leonard et al. (2001), the model fronts are equatorward extensions of the subtropical front while at the southernmost phase of its annual cycle.

An additional point of comparison between the model and the observations can be drawn from the frequency and wavenumber power spectra in the model and in the WHOTS data (Fig. 7). In the model, the slope of the *wavenumber* power spectrum increases from -2.2 at 50 m to -3.4 at 150 m (Fig. 7b). This is in agreement with theory and previous numerical studies that show a transition from unbalanced flows and a slope of -2 near the surface to balanced flows and a slope of -3 in the interior (*e.g.* Capet et al., 2008). Lacking observations of the wavenumber spectrum, we compare the observed *frequency* spectrum to that from the model. In the SML, the two agree with respect to both slope (-2.0) and level. Below the SML, near 150 m, the model frequency spectrum is steeper (-2.7) than that from WHOTS (-2.4), and has roughly one tenth of the variance. This is consistent with the model's too rapid decay with depth of its first EOF mode for potential density.

Can we infer information on the dynamics based on frequency spectra? Ferrari and Wunsch (2010) highlight the difficulty in extracting dynamical information from frequency spectra. Slopes of wavenumber and frequency spectra are expected to be the same for a specific regime of quasi-geostrophic turbulence but it is not clear how this applies to the ocean. The present model suggests that, for the region and depth range considered, the slope differs between the wavenumber and frequency spaces. A similar result has been found over various regions from the analysis of idealized quasi-geostrophic turbulence simulations, realistic ocean general circulation models and satellite SSH (Arbic et al., 2012). Additional understanding of the change of slope between the wavenumber and frequency spaces in a regime dominated by either surface or interior quasi-geostrophy would be needed to exploit the WHOTS frequency spectra and infer reliable information on the dynamics.

References

Anderson, L.A., 1995. On the hydrogen and oxygen content of marine phytoplankton. Deep-Sea Res. I 42, 1675–1680, http://dx.doi.org/10.1016/0967-0637(95)00072-E.

Arbic, B.K., Scott, R.B., Flierl, G.R., Morten, A.J., Richman, J.G., Shriver, J.F., 2012. Nonlinear cascades of surface oceanic geostrophic kinetic energy in the frequency domain. J. Phys. Oceanogr. 42, 1577–1600, http://dx.doi.org/10.1175/JPO-D-11-0151.1.

Boccaletti, G., Ferrari, R., Fox-Kemper, B., 2007. Mixed layer instabilities and restratification. J. Phys. Oceanogr. 37, 2228–2250, http://dx.doi.org/10.1175/JPO3101.1.

Canuto, V.M., Howard, A., Cheng, Y., Dubovikov, M.S., 2001. Ocean turbulence. Part I: one-point closure model-momentum and heat vertical diffusivities. J. Phys. Oceanogr. 31, 1413–1426, http://dx.doi.org/10.1175/1520-0485(2001)031<1413:OTPIOP>2.0.CO;2.

Canuto, V.M., Howard, A., Cheng, Y., Dubovikov, M.S., 2002. Ocean turbulence. Part II: vertical diffusivities of momentum, heat, salt, mass, and passive scalars. J. Phys. Oceanogr. 32, 240–264, http://dx.doi.org/10.1175/1520-0485(2002)032<0240:OTPIVD>2.0.CO;2.

Capet, X., McWilliams, J.C., Molemaker, M.J., Shchepetkin, A.F., 2008. Mesoscale to submesoscale transition in the California current system. Part I: Flow structure, eddy flux, and observational tests. J. Phys. Oceanogr. 38, 29–43, http://dx.doi.org/10.1175/2007JPO3671.1.

Carter, G.S., Merrifield, M.A., Becker, J.M., Katsumata, K., Gregg, M.C., Luther, D.S., Levine, M.D., Boyd, T.J., Firing, Y.L., 2008. Energetic of M2 barotropic-to-baroclinic tidal conversion at the Hawaiian Islands. J. Phys. Oceanogr. 38, 2205–2223, http://dx.doi.org/10.1175/2008JPO3860.1.

Chelton, D.B., Schlax, M.G., Samleson, R.M., 2011. Global observations of nonlinear mesoscale eddies. Prog. Oceanogr. 91, 167–216, http://dx.doi.org/10.1016/j.pocean.2011.01.002.

Chen, S., Qiu, B., 2010. Mesoscale eddies northeast of the Hawaiian archipelago from satellite altimeter observations. J. Geophys. Res. 115, C03016, http://dx.doi.org/10.1029/2009JC005698.

Church, M.J., Mahaffey, C., Letelier, R.M., Lukas, R., Zher, J.P., Karl, D.M., 2009. Physical forcing of nitrogen fixation and diazotroph community structure in the North Pacific subtropical gyre. Global Biogeochem. Cycles 23, GB2020, http://dx.doi.org/10.1029/2008GB003418.

Falkowski, P.G., Ziemann, D., Kolber, Z., Bienfang, P.K., 1991. Role of eddy pumping in enhancing primary production in the ocean. Nature 352, 55–58, http://dx.doi.org/10.1038/352055a0.

Ferrari, R., Wunsch, C., 2010. The distribution of eddy kinetic and potential energies in the global ocean. Tellus 62A, 92–108, http://dx.doi.org/10.1111/j.1600-0870.2009.00432.x.

Jia, Y., Calil, P.H.R., Chassignet, E.P., Metzger, E.J., Potemra, J.T., Richards, K.J., Wallcraft, A.J., 2011. Generation of mesoscale eddies in the lee of the Hawaiian Islands. J. Geophys. Res. 116, C11009, http://dx.doi.org/10.1029/2011JC007305.

Johnson, K.S., Riser, S.C., Karl, D.M., 2010. Nitrate supply from deep to near-surface waters of the North Pacific subtropical gyre. Nature 465, 1062–1065, http://dx.doi.org/10.1038/nature09170.

Karl, D.M., Lukas, R., 1996. The Hawaii Ocean Time-series (HOT) program: Background, rationale, and field implementation. Deep-Sea Res. II 43, 129–156, http://dx.doi.org/10.1016/0967-0645(96)00005-7.

Karl, D.M., Letelier, R.M., Tupas, L.M., Dore, J.E., Christian, J.R., Hebel, D.V., 1997. The role of nitrogen fixation in the biogeochemical cycling in the subtropical North Pacific Ocean. Nature 388, 533–538, http://dx.doi.org/10.1038/41474.

Karl, D.M., Björkman, K.M., Dore, J.E., Fujieki, L., Hebel, D.V., Houlihan, T., Letelier, R.M., Tupas, L.M., 2001. Ecological nitrogen-to-phosphorus stoichiometry at station ALOHA. Deep-Sea Res. II 48, 1529–1566, http://dx.doi.org/10.1016/S0967-0645(00)00152-1.

Karl, D.M., Bates, N.R., Emerson, S., Harrison, P.J., Jeandel, C., Llinás, O., Liu, K.-K., Marty, J.-C., Michaels, A.F., Miquel, J.C., Neuer, S., Nojiri, Y., Wong, C.S., 2003. Temporal studies of biogeochemical processes determined form ocean time-series observations during the JGOFS era. In: Fasham, M.J.R. (Ed.), Ocean Biogeochemistry. Springer, Berlin, pp. 239–267, Chapter 10.

Karl, D.M., Bidigare, R.R., Church, M.J., Dore, J.E., Letelier, R.M., Mahaffey, C., Zehr, J., 2008. The nitrogen cycle in the North Pacific Trades biome: an evolving paradigm. In: Capone, D.G., Carpenter, E.J., Mulholland, M., Bronk, D.A (Eds.), Nitrogen in the Marine Environment. Elsevier, Amsterdam, pp. 705–769, Chapter 16.

Klein, P., Lapeyre, G., 2009. The oceanic vertical pump induced by mesoscale and submesoscale turbulence. Ann. Rev. Mar. Sci. 1, 351–375, http://dx.doi.org/10.1146/annurev.marine.010908.163704.

Körtzinger, A., Schimanski, J., Send, U., 2005. High quality oxygen measurements from profiling floats: a promising new technique. J. Atmos. Ocean. Technol. 22, 302–308, http://dx.doi.org/10.1175/JTECH1701.1.

Lapeyre, G., Klein, P., 2006. Impact of the small-scale elongated filaments on the oceanic vertical pump. J. Mar. Res. 64, 835–851, http://dx.doi.org/10.1357/002224006779698369.

Leonard, C.L., Bidigare, R.R., Seki, M.P., Polovina, J.J., 2001. Interannual mesoscale physical and biological variability in the North Pacific central gyre. Prog. Oceanogr. 49, 211–225, http://dx.doi.org/10.1016/S0079-6611(01)00024-6.

Letelier, R.M., Karl, D.M., 1998. Trichodesmium spp. physiology and nutrient fluxes in the North Pacific Subtropical Gyre. Aquat. Microbial Ecol. 15, 265–276, http://dx.doi.org/10.3354/ame015265.

Letelier, R.M., Karl, D.M., Abbott, M.R., Flament, P., Freilich, M., Lukas, R., Strub, T., 2000. Role of late winter mesoscale events in the biogeochemical variability of the upper water column of the North Pacific Subtropical Gyre. J. Geophys. Res. 105, 28723–28739, http://dx.doi.org/10.1016/S0967-0645(01)00108-4.

Lévy, M., Klein, P., Treguier, A.-M., 2001. Impact of sub-mesoscale physics on production and subduction of phytoplankton in an oligotrophic regime. J. Mar. Res. 59, 535–565, http://dx.doi.org/10.1357/002224001762842181.

Lévy, M., 2008. The modulation of biological production by oceanic mesoscale turbulence. In: Lecture Notes in Physics, vol. 744, pp. 219–261, doi: 10.1007/978-3-540-75215-8_9.

Lévy, M., Ferrari, R., Franks, P.J.S., Martin, A.P., Rivière, P., 2012. Bringing physics to life at the submesoscale. Geophys. Res. Lett. 39, L14602, http://dx.doi.org/10.1029/2012GL052756.

Martin, A.P., Pondaven, P., 2003. On estimates for the vertical nitrate flux due to eddy pumping. J. Geophys. Res. 108, 3359, http://dx.doi.org/10.1029/2003JC001841.

Mahadevan, A., Tandon, A., 2006. An analysis of mechanisms for submesoscale vertical motion at ocean fronts. Ocean Modelling 14, 241–256, http://dx.doi.org/10.1016/j.ocemod.2006.05.006.

McGillicuddy Jr, D.J., Robinson, A.R., 1997. Eddy-induced nutrient supply and new production in the Sargasso Sea. Deep-Sea Res. I 44, 1427–1450, http://dx.doi.org/10.1016/S0967-0637(97)00024-1.

McGillicuddy Jr, D.J., Robinson, A.R., Siegel, D.A., Jannasch, H.W., Johnson, R., Dickey, T.D., McNeil, J., Michaels, A.F., Knap, A.H., 1998. Influence of mesoscale eddies on new production in the Sargasso Sea. Nature 394, 263–266, http://dx.doi.org/10.1038/28367.

McGillicuddy Jr, D.J., Anderson, L.A., Doney, S.C., Maltrud, M.E., 2003. Eddy-driven sources and sinks of nutrients in the upper ocean: Results from a 0.1° resolution model of the North Atlantic. Global Biogeochem. Cycles 17 (2), 1035, http://dx.doi.org/10.1029/2002GB001987.

Nolan, K., 2008. Characteristics and water properties of mesoscale eddies in the region of Station ALOHA, Master Thesis, University of Hawaii at Manoa, p. 279.

Nurser, A.J.G., Zhang, J.W., 2000. Eddy-induced mixed layer shallowing and mixed layer/thermocline exchange. J Geophys. Res. 105, 21,851–21,868, http://dx.doi.org/10.1029/2000JC900018.

Oschlies, A., 2008. Eddies and upper-ocean nutrient supply. In: Hecht, M., Hasumi (Eds.), Ocean Modeling in an Eddying Regime. Geophysical Monograph Series 177. AGU, Washington, D.C, pp. 115–130, http://dx.doi.org/10.1029/177GM09.

Redfield, A.C., Ketchum, B.H., Richards, F.A., 1963. The influence of organisms on the composition of seawater. In: Hill, M.N. (Ed.), The Sea, Ideas and Observations on Progress in the Study of the Seas, vol. 2. Interscience, New York, pp. 26–77.

Sakamoto, C.M., Johnson, K.S., Coletti, L.J., 2009. Improved algorithm for the computation of nitrate concentrations in seawater using an in situ ultraviolet spectrophotometer. Limnol. Oceanogr.: Methods 7, 132–143, http://dx.doi.org/10.4319/lom.2009.7.132.

Siegel, D.A., McGillicuddy Jr., D.J., Fields, E.A., 1999. Mesoscale eddies, satellite altimetry, and new production in the Sargasso Sea. J. Geophys. Res. 104, 13,359–13,379, http://dx.doi.org/10.1029/1999JC900051.

Singler, H.R., Villareal, T.A., 2005. Nitrogen inputs into the euphotic zone by vertically migrating Rhizosolenia mats. J. Plankton Res. 27, 545–556, http://dx.doi.org/10.1093/plankt/fbi030.

Spall, S.A., Richards, K.J., 2000. A numerical model of mesoscale frontal instabilities and plankton dynamics – I. Model formulation and initial experiments. Deep-Sea Res. I 47, 1261–1301, http://dx.doi.org/10.1016/S0967-0637(99)00081-3.

Sutka, R.L., Ostrom, N.E., Ostrom, P.H., Phanikumar, M.S., 2004. Stable nitrogen isotope dynamics of dissolved nitrate in a transect from the north Pacific subtropical gyre to the eastern tropical north Pacific. Geochim. Cosmochim. Acta 68, 517–527, http://dx.doi.org/10.1016/S0016-7037(03)00483-6.

Thomas, L.N., Tandon, A., Mahadevan, A., 2008. Submesoscale processes and dynamics. In: Hecht, M., Hasumi, H. (Eds.), Ocean Modeling in an Eddying Regime. Geophysical Monograph Series 177. AGU, Washington, D.C, pp. 17–38, http://dx.doi.org/10.1029/177GM04.

Tu, C.-C., Chen, Y.-L., 2011. Favorable conditions for the development of a heavy rainfall event over Oahu during the 2006 wet period. Weather Forecast. 26, 280–300, http://dx.doi.org/10.1175/2010WAF2222449.1.

von Storch, H., Zwiers, F.W., 1999. Statistical Analysis in Climate Research. Cambridge University Press, Cambridge, 484pp.

Zhao, Z., Alford, M.H., Girton, J., Johnston, T.M.S., Carter, G., 2011. Internal tides around the Hawaiian Ridge estimated from multisatellite altimetry. J. Geophys. Res. 116, C12039, http://dx.doi.org/10.1029/2011JC007045.